Proceedings of ASME Turbo Expo 2002:
"Gas Turbines for a Better Tomorrow"
03-06 June 2002, Amsterdam, The Netherlands

GT-2002-30214

COMBINED 3D FLOW AND HEAT TRANSFER MEASUREMENTS IN A 2-PASS INTERNAL COOLANT PASSAGE OF GAS TURBINE AIRFOILS

D. Chanteloup / denis.chanteloup@epfl.ch / EPFL – LTT – 1015 Lausanne – Switzerland
Y. Juaneda / juaneda@imft.fr / EPFL – LTT – 1015 Lausanne – Switzerland
A. Bölcs / albin.boelcs@epfl.ch / EPFL – LTT – 1015 Lausanne – Switzerland

ABSTRACT

A study of the flow and heat transfer in a stationary model of a two-pass internal coolant passage is presented, which focuses on the flow characteristic effects on the wall heat transfer distribution. Results are given in the upstream fully developed region.

Heat transfer measurements were made with a transient technique using thermochromic liquid crystal technique to measure a surface temperature. The technique allows full surface heat transfer coefficient measurements on all the walls. Flow measurements were made with a stereoscopic digital PIV system, which measures all three-velocity components simultaneously.

The coolant passage model consists of two square ducts, each having a 20 hydraulic diameter length. The ducts are connected by a sharp 180º bend with a rectangular outer wall. 45º ribs are mounted in a staggered arrangement on the bottom and top walls of both legs. The height of the ribs is equal to 0.1 hydraulic diameters. They are spaced 10 rib heights apart. The flow and heat transfer measurements were obtained at one flow condition with an inlet flow Reynolds number, based on the hydraulic diameter, of 50,000.

The paper presents detailed measurement results of the flow characteristics and of the heat transfer distribution in the upstream straight leg of the passage and describes how the main and secondary flows influence the heat transfer distribution in the fully developed regions of the channel.

INTRODUCTION

For the design of gas turbine blades, a detailed knowledge of the physical phenomena in the passage is necessary. To improve the performance of the CFD codes, a validation of the predictions is necessary, and detailed measurements of the flow structure and heat transfer distribution in the passages are required for comparison.

Rib arrays inside an internal cooling channel are often used in heat exchanger systems to enhance the heat transfer rate. When ribs are oblique to the channel, the main flow can more easily climb over the ribs and generate stronger secondary flow, as shown in Schabacker, J. (1998). Heat transfer characteristics have been measured in 45deg rib arrangement in literature. Several references describe area averaged results, performed mainly with thermocouples (Mochizuki, S. (1997) and Han, J. C. (1991)). Correlations presented in Han, J. C. (1988) and Han, J. C. (1987), have been built in single pass channel for several Re numbers and geometrical characteristics. Detailed full surface heat transfer measurements are also published. Some results are compared to flow measurements in the vicinity of the walls (Wang, Z. (1996)). Rau, G. (1998) showed the impact of rib pitch parameter in channels with a parallel 45deg rib arrangement. Studies of the flow characteristics in the coolant channels. Schabacker, J. (1999) and Schabacker, J. (1998), showed velocity (PIV) measurements in the turn region of 2-pass coolant channels. Bonhoff, B. (1998) and Hermanson, K. (2000) showed the capability of CFD codes to simulate flow characteristics and heat transfer in ribbed channels.

Although detailed heat transfer measurements in coolant channels are available in literature, to the authors knowledge, the direct combination of flow measurements and heat transfer distribution in such ducts has not been described. In the present study, the particle-image-velocimetry (PIV) measurement method was employed for the investigation of the flow field in models of a stationary two-pass coolant passage. The measurement error introduced in high 3D flows, can be avoided by using a stereoscopic PIV setup. A stereoscopic digital PIV system, based on the angular displacement method, was used for the present investigation (Schabacker, J. (1996)). This PIV system measures all three instantaneous velocity components. Subsequently, an ensemble average of the velocity data, in

identical spatial windows, is calculated to determine the mean and fluctuating velocity field.

Full surface heat transfer measurements were made on all the outer walls of the channel. The transient liquid crystal technique described in Wang, Z. (1996), is suitable for full surface heat transfer measurements in regions with high heat transfer gradients. Because in long test channels, the gas temperature is not a perfect step, the Duhamel theorem was used to process the gas temperature (Ekkad, S. V. (1995)). The information was processed with a full digital system as presented in Vogel, G. (2000).

This paper presents initial results from the Brite-Euram project, for Internal Cooling of Turbine Blades (ICTB). The main objective of Chanteloup, D. (2001) was to present flow results in the present configuration. The specific objectives of the present paper are to determine and present the influence of the flow characteristics on the heat transfer distribution in the fully developed region of a 2-pass coolant channel with a 45deg rib arrangement.

NOMENCLATURE

X	Cartesian coordinate in axial duct direction
Y	Cartesian coordinate in cross duct direction
Z	Cartesian coordinate in horizontal duct direction
U	Mean velocity component in x direction
V	Mean velocity component in y direction
W	Mean velocity component in z direction
U_b	Bulk mean-velocity
L	Test section length
D	Height and width of passage legs, D=100 mm
D_H	Hydraulic diameter D_h=D
B	Thickness of divider plate
P	Rib pitch
e	Rib height
S	Section length in bend at 90° section
α	Heat transfer coefficient
λ	Plexiglas thermal conductivity
$\Lambda = \lambda/(\rho \cdot C_p)$	Plexiglas thermal diffusivity
$T = (T_{LC} - T_i)/(T_G - T_i)$	dimensionless temperature
$f = \frac{\Delta P}{L} \cdot \frac{D_H}{\frac{1}{2}\rho U_{b,in}^2}$	friction factor
Nu	Nusselt number
$St = Nu/(\mathrm{Re} \cdot \mathrm{Pr})$	Stanton number

EXPERIMENTAL SETUP

Test Facility

A sketch of the test section is shown in Figure 1 and geometry characteristics are given in Table 1. Air was the working medium and was supplied by a continuously running compressor. The air enters the settling chamber with an inner diameter of 600mm via a 150mm tube and a conical entrance section with an angle of 30deg. The settling chamber is equipped with a combination of perforated plates, honeycombs and meshes to reduce unsteadiness and swirl in the flow. A bell mouth entry leads the air from the settling chamber to the test channel. The settling chamber outlet is equipped with heaters for heat transfer measurements. During the flow measurements, the heaters are removed form the channel. A turbulence grid is placed downstream of the heaters in both flow and heat transfer measurements to reach the same turbulence level at the channel inlet.

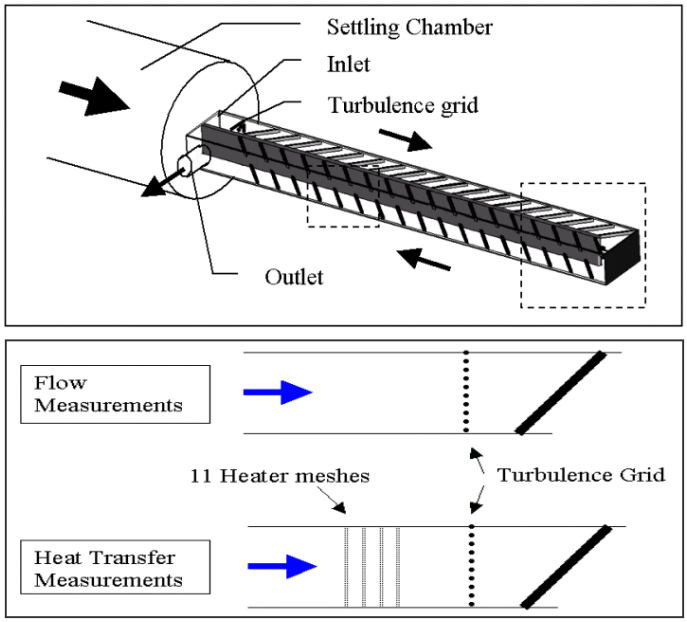

Figure 1: The internal coolant passage test facility and inlet region details.

Test section length	L	20 D_h
Height & Width of passage legs	D	1 D_h
Bend cross section	S	1 D_h
Length of divider plate		19 D_h
Thickness of divider plate	B	0.2 D_h
Rib cross-section		0.01D_h^2
Rib pitch	P	1 D_h
Rib height	e	0.1 D_h
Rib angle of attack		45deg

Table 1: The coolant passage geometry characteristic.

The test section is a two-pass, cooling passage model of a gas turbine blade. The flow path in the downstream and upstream passages has a cross-section of 100*100mm^2 with a corresponding hydraulic diameter, $D_H = 100mm$, and a length of $20D_H$. The outer walls of the test section are made of 5mm-thick extruded Plexiglas to obtain good optical properties for

the PIV experiment. In the straight-corner bend, the clearance between the tip of the divider plate and the outer wall is equal to 1 Dh. The thickness of the divider plate or web between the two passages is $0.2D_H$. The tip of the divider plate is cylindrically shaped with a $0.1D_H$ radius. Square ribs with an angle of 45 deg to the passage centreline, rib heights of 0.1 hydraulic diameters ($e/D_H = 0.1$), and rib spacing of 10 rib heights ($P/e = 10$) are mounted in a staggered arrangement on the top and bottom wall of the passage. The ribs in the bend region and the dimensions of the bend are shown in Fig 2. Eighteen ribs are mounted on each of the top and bottom walls in each of the upstream and downstream passages of the model (18 * 4).

A modular concept was chosen for the test section that allows an easy exchange of the components. The total model test section including the test section entrance is turned 90 deg around the x-axis to obtain additional measurement planes without changing the flow conditions in the passage. This allows an easy optical access to the positions of interest for the PIV measurements.

Flow conditions, measurement program and coordinate systems

The measurements were obtained with air as working medium, at a flow Reynolds number of 50,000 (corresponding to a bulk velocity: $Ub = 7.58m/s$), at the entrance of the test section. The Reynolds number is based on the 0.1 m hydraulic diameter with an air temperature of 18 C. Upstream of the test-rig, the mass flow is measured by means of a 5864S Brooks flow meter with a 1-percent accuracy. The turbulence level is approximately 3 percent at the model inlet. An experimental study was conducted to assess the effect of varying test section orientation on the flow. The small variations between the flow conditions are within the measurement uncertainty and can therefore be neglected for the experiments.

Static pressure measurements in the configurations have been performed with a DRUCK LPM 5480 differential pressure transmitter, with a 6N/m^2-accuracy.

Detailed measurements of the flow structure in the passage have been obtained in the bend, upstream ($3D_H$) and downstream ($4D_H$) of the 180 deg bend. A total of twenty-four measurement planes provided with nine hundred measurement points (30 by 30), were taken in the region of interest. Fifteen planes parallel to the Y-axis and nine planes parallel to the XZ-plane allowed to give a description of the 3D flow field in the fully developed region. An interpolation of all planes, based on an inverse distance algorithm, allowed obtaining streamlines from measured data in the entire volume, as shown in Figure 1.

The definition of the coordinate systems in the test facility is shown in Figure 2. A Cartesian coordinate system is used for the straight passages and a cylindrical coordinate system is used for the bend region. The origin for both coordinate systems is set on the bottom wall at the centre of the rounded end of the divider plate. In the Cartesian (*X, Y, Z)* system, *X* is defined as positive in the streamwise direction of the flow downstream of the bend exit, *Y* is defined positive vertically upwards in the horizontal test section orientation, and *Z* is defined as shown.

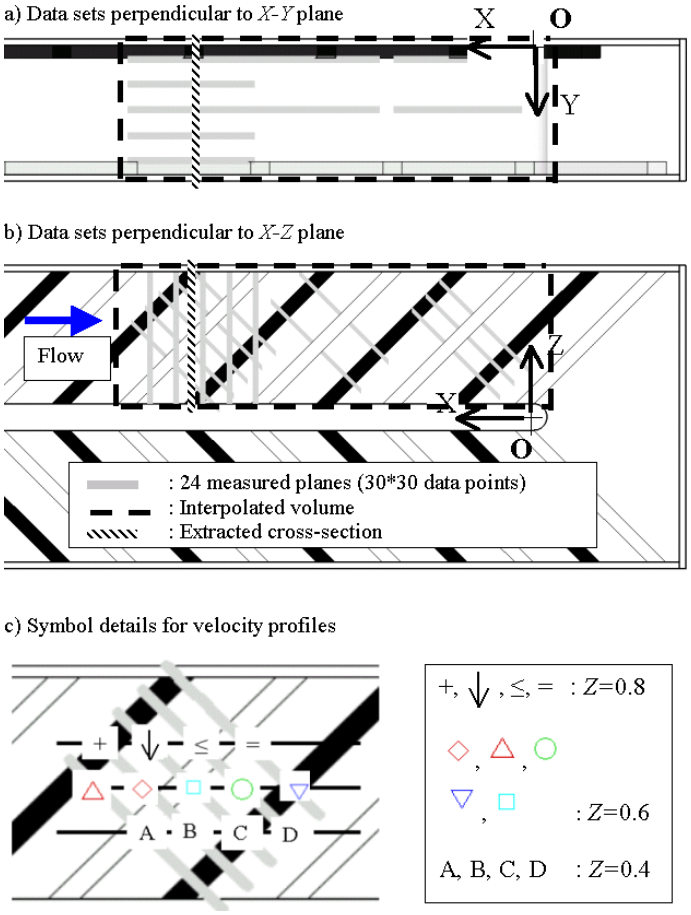

Figure 2: Measurement sections. The symbols represent the measurement lines (Y direction) that will be analysed in the next sections (Figure 5).

Flow measurements

Particle image Velocimetry (PIV) was chosen as a flow measurement technique. A homemade stereoscopic PIV system was used, which allowed to obtain the mean velocity fields as well as the turbulence quantities in approximately a hundred planes in each test configuration.

Di-Ethyl-Hexyl-Sebacate (DEHS) from TOPAS is used as light scattering droplets for the PIV experiments. A DLR- made Aerosol Generator using Laskin Nozzles generates 1-3 µm-diameter DEHS droplets. The droplets are injected upstream of the settling chamber to guarantee a homogeneous seeding density in the test section.

A 1.2-mm thick light sheet that illuminates the particles is created by a Quantel Twins B Nd-Yag double oscillator pulsed laser. A plano-concave lens (-30mm focal length) combined

with two plano-cylindrical lenses (76.2 and 300mm focal length) transform the beam into the vertical light sheet.

The imaging system consists of two independent Kodak ES1.0 cameras, each having its own PC. A Nikon Nikkor 55mm lens is mounted on each camera. For a typical recording situation, the cameras are placed with an oblique angle of 4.3º at a distance of 0.7m from the light sheet plane. The pulse separation time is about 40µs. The frame grabber is an Imaging Technology PCI frame grabber with 2 MB memory onboard. During the PIV measurement series, 10 images are written in real time into the PC's RAM memory and subsequently saved on the hard disk. The automation of the process allows storing of 5000 frames per measurement plane. The laser components (flash lamp and Q-switch) and the cameras are triggered by 10Hz TTL signals that are dispatched to all the elements with specific delays.

The 3D PIV measurements are obtained from the combination of two 2-dimensional vector fields. From the processed vector fields, the instantaneous three-dimensional velocity field can be reconstructed. Matlab homemade reconstruction software was developed at the EPFL-LTT. With angular PIV systems, where both cameras observe the light sheet from the same side, the corresponding interrogation positions in the right and left images do not match in general. Therefore, a calibration of the camera system is performed which also corrects for the distortion of the images in the lenses and the Plexiglas walls of the passage. In order to obtain PIV measurements in the presented forms, the statistical distribution of the velocity components is determined in identical spatial windows from a series of instantaneous PIV measurements. From these statistical distributions, the ensemble average is calculated to determine the desired mean-velocity field.

Heat transfer measurements

For the present study, transient heat transfer experiments were performed using liquid crystals to determine the surface temperature. The transient technique is well described in Wang, Z. (1991). The transient liquid crystal technique consists of monitoring the surface temperature evolution in time with a step change in the gas temperature. Eleven fine, fast response, mesh heaters were fitted to the duct inlet to produce the step change in gas temperature. This heater comprises a mesh of stainless steel wires, 40µm in diameter woven at a pitch of approximately 100µm, with an open area of 38% (see Wang, Z. (1996) for more details). The meshes were connected in series to the 10kW power supply (256A, 40V). Figure 3 shows a typical variation of temperature with time in the test channel. At the inlet, the heaters provide a step change in temperature of 75% and 99% of the total temperature increase, in 0.4s and 0.6s respectively. The temperature distribution across the inlet section is constant with a spatial variation of less than 3% of the total temperature step.

In the present experiments, the heat transfer coefficient α is obtained by using the 1D unsteady heat conduction equation, and treating the wall material as "semi-infinite" which limits the allowable measurement time. Vogel, G. (2001) showed, that the maximum allowable measurement time can be calculated from $t_{max} = L^2/(0.25 \cdot \Lambda)$, where L is the model thickness and Λ the thermal diffusivity of the model material. In the present study, a 5mm thick Plexiglas model was used to obtain good optical properties for PIV experiments; the maximum allowable time is $t = 64s$, which is longer than the typical measurement duration of $38s$.

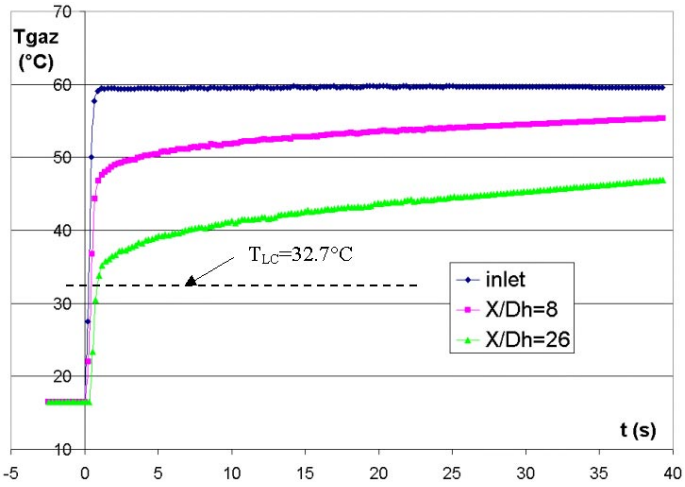

Figure 3: Gas temperature increase at different X/D *locations for heat transfer post processing*

The transient heat transfer measurement method consists of monitoring the surface temperature evolution by acquiring the colour signal of a liquid crystal coating applied on the test section. By using a single layer of narrow-band thermo-chromic liquid crystals (Hallcrest BM/R30.5C0.7W/C17-10), the evolution of the local surface temperature $T_{wall}(y,z,t)=T_{LC}$ is obtained from a hue capturing technique. Several miniature colour CCD cameras mounted around the test section record the colour change of the liquid crystal coating. The video signal of each view is digitally stored on DV (Digital Video) tapes. The use of the DV format storage ensures precise colour image signal restitution at constant image frequency and without any noise generation. Video sequences of each camera are transferred subsequently to a computer where the image processing and the data reduction are performed.

The liquid crystals are painted directly on the channel inner Plexiglas surface. A black paint coating covers the liquid crystals to provide a good colour background for image acquisition. A validation procedure was conducted to ensure that the black coating doesn't affect the quality of the results.

The 1-D transient conduction equation, with classical initial conditions and boundary conditions on the test surface, is used to obtain the non-dimensional temperature at the convective boundary surface:

$$\frac{T_{wall}(t) - T_i}{T_G - T_i} = 1 - \exp^{\alpha^2 \frac{\Lambda \cdot t}{\lambda^2}} \; erfc\left(\frac{\alpha\sqrt{\Lambda \cdot t}}{\lambda}\right) \qquad (1)$$

The initial temperature T_i was measured in the Plexiglas model, after a thermal balance was reached between the gas temperature and the model outer surface temperature.

Thermocouples were placed along the channel to measure the gas temperature. They were located in the centre of one of the secondary flow vortex ($Y = 0.67$, $Z = 0.43$ in the upstream leg). Tests based on numerical simulations showed that at this cross-section location, the gas temperature is closer to the bulk temperature than the centreline temperature, with $|T_{measured} - T_{bulk}| < 1°C$ along the entire channel. The thermocouples were separated $1D_H$ from another in the region of interest. A linear interpolation of the gas temperature in X direction was performed for every location between the thermocouples.

The use of heater grids yields a double dependence of the gas temperature on time and X-location (see Figure 3). Downstream of the inlet, due to heat exchange the temperature increase is no longer a step. For a given X, the gas temperature is an increasing function of time (Ekkad, S. V. (1995)). It can be shown that, when the gas temperature change can be expressed as series of n summed step functions, the Plexiglas surface temperature $T_{wall}(t) = T_{LC}$ is

$$T_{wall}(t) = T_{LC} = T_i + \sum_{j=1}^{n} (T_{G,j} - T_{G,j\_1}) \cdot F(t - t_j) \tag{2}$$

with

$$F(t - t_j) = \left\{ 1 - \exp^{\alpha^2 \frac{\Lambda \cdot (t - t_j)}{\lambda^2}} \; erfc\left(\frac{\alpha \sqrt{\Lambda \cdot (t - t_j)}}{\lambda} \right) \right\} \tag{3}$$

An iterative procedure is used to determine the value of the heat transfer coefficient from the above equations.

PIV uncertainty analysis

Schabacker, J. (1996), Schabacker, J. (1998), Schabacker, J. (1998) demonstrated the applicability of the presented stereoscopic PIV technique in details. Using the method of Bendat, J.S. (1986), the mean value of the measured velocities is calculated by taking the instantaneous velocity measurements of the sample, summing the values, and dividing by the number of samples ($N = 1250$ per measurement plane in the present study):

$$\bar{x} = \frac{1}{N} \sum_{i=1}^{N} x_i \tag{4}$$

In a similar manner, a measure of the fluctuating velocities can be obtained from the sample variance:

$$s^2 = \frac{1}{N-1} \sum_{i=1}^{N} (x_i - \bar{x})^2 \tag{5}$$

In the equations x and s^2 are the *sample mean* and *sample variance*, respectively. The number of observations N used to compute the estimates is called the *sample size*. Using the method of Bendat, J.S. (1986) The uncertainty for the mean velocity values of the present measurements is of order of 1 percent with a confidence level of 95 percent. The uncertainty of the mean velocity depends on the normal stresses and as a consequence is higher in regions where the turbulence level is high. The uncertainty level of the normal stresses of the Reynolds tensor, with a confidence level of 95 percent, is 8 percent of the normal stress values. The uncertainty of the normal stresses depends only on the number of samples and on the confidence level. Further details of the uncertainty method are given in Schabacker, J. (1998).

Heat transfer uncertainty analysis

The error in the heat transfer measurements has been calculated considering the method described in Höcker, R. (1996). It showed that the error can be minimised by adjusting measurement parameters as the model material and the dimensionless temperature $T = (T_{LC} - T_i)/(T_G - T_i)$. In the present study, the heat transfer coefficients are of the order of $20 W/m^2K$ to $200 W/m^2K$. Using the method of Höcker, R. (1996), this leads to optimum dimensionless temperatures between $0.2 < T < 0.4$. Thus it was chosen to set the different temperature at $T_i \approx 18°C$, $T_G \approx 70°C$, $T_{LC} \approx 32.7°C$, in order to obtain an average dimensionless temperature $T = 0.28$. The maximum error can be estimated to $\pm 8\%$ on the heat transfer coefficient under the assumption that the heat transfer coefficient is constant during the experiment.

RESULTS AND DISCUSSION

The objectives of the present paper are:

- to present complete flow and heat transfer sets of data in the fully developed region of a 2-pass internal coolant channel.
- to relate the flow and heat transfer distributions in a coolant channel with 45deg ribs.
- to show how the vortex structure influences the heat transfer distribution in the fully developed region of a 2-pass coolant channel with 45deg rib arrangements.

Flow characteristics

A comparison of velocity components in the developed flow region of a similar coolant passage was presented by Bonhoff, B. (1998). The measurements showed that the flow with a 45-deg rib arrangement differs from the flow in a similar passage with a 90-deg rib arrangement Schabacker, J. (1999). With 90 deg ribs, a developed flow condition in terms of mean velocity and turbulent kinetic energy was achieved after 3 rib modules. The flow in the passage with 45deg rib arrangement requires a longer development length; at least 8 rib modules are needed to achieve a developed flow condition for the mean velocity components and 12 rib modules are required for the turbulent kinetic energy of the flow. In the present

configuration, 18 rib-modules are placed in the upstream leg, to produce a developed flow field before the 180-deg bend.

The velocity components downstream of the 16th rib module are judged to be in a developed flow region.

Table 2 shows a comparison between the present channel friction factor and a correlation for 45deg rib-arrangements presented in Han, J. C. (1988) (Han). The correlation was extrapolated beyond Han's test range ($0.047 < e/D_H < 0.078$). The result from the present study is an average of measurements in the fully developed section of the first leg. The Han correlation is 30% lower than the present results. Measurements and numerical simulations of Haasenritter, A. (2001) showed a friction factor approximately equal to that measured in the present study. The differences with the Han, J. C. (1988) correlation are thought to be due to geometrical differences between the test channels, especially the rib height and blockage ratio.

Re= 50 000	**Results**	**Han**
f	0.066	0.047

Table 2:Fully developed friction factor compared to Han, J. C. (1988) correlation.

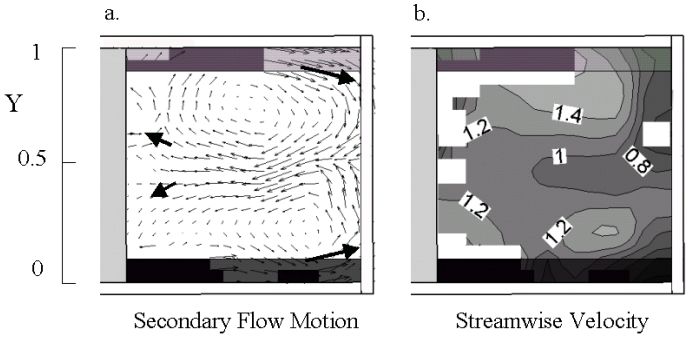

Figure 4: Streamwise and secondary flow motion in a fully developed flow cross section of a coolant channel with 45deg rib arrangement.

It has been shown (Chanteloup, D. (2001) and Schabacker, J. (1999)), that the vortices behind inclined ribs move along the ribs and then join the main flow. This interaction between main flow and rib-induced vortices causes a strong secondary flow motion in the passage leg. The secondary flow consists of two counter-rotating vortices that drive fluid from the duct centre towards the web along the centre plane and to the sidewall along the ribbed walls as shown in Figure 4. Note that the web is placed on the right hand side of the figure.

It was shown in Chanteloup, D. (2001), that the secondary flow field impinges on two main areas in the channel. Flow with velocity as high as $0.3U_b$ impinges on the outer wall at approximately one rib height above the ribbed walls ($Y = 0.15$ and $Y = 0.85$). Flow with lower velocities ($0.1U_b$) impinges on the web among the centre plane $Y = 0.5$. The streamwise velocity characteristics in Figure 6 b., shows three regions of high streamwise velocity. Two are located in the secondary vortex core. The third is less obvious and is located adjacent to the web, and limits the impingement velocity of the secondary flow.

The streamwise (U), cross-stream (W) and normal (V) velocity profiles at selected streamwise and cross-stream locations are shown in Figure 5. The streamwise locations are between $X = 2.1$ and 3.1 (All the distances are normalized by D_H). The cross-stream locations are at $Z = 0.4$, 0.6 and 0.8. Note that the web wall location is at $Z = 0.1$. Data from values of $Y = 0.06$ to 0.94 are plotted except at the rib surfaces where the closest value of has a $\Delta Y = 0.06$. The measurement procedures with this PIV set of optics has a probe dimension of $\Delta Y = 0.06$. For Y values closer than 0.06 to the wall, spurious results were obtained due to wall light reflections.

a. Overview of the graphs in the next figure

Z	**Streamwise Velocity**	**Cross-stream Velocity**	**Vertical Velocity**
0.4	a.1.	b.1.	c.1.
0.6 (passage center)	a.2.	b.2.	c.2.
0.8	a.3.	b.3.	c.3.

b. Velocity profiles

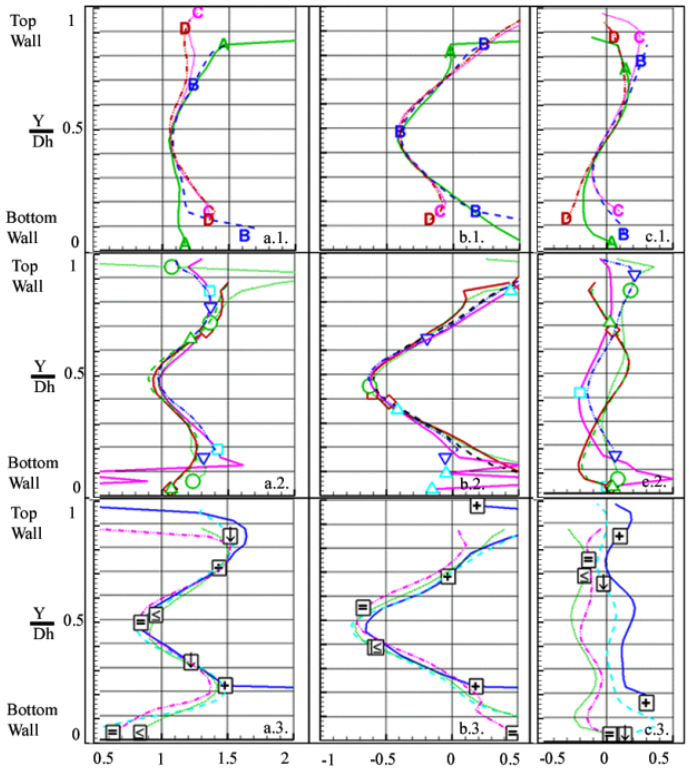

Figure 5: Velocity profiles in the 16th rib module, normalized by Ub. See Figure 2 for exact locations in the rib module.

The streamwise velocity profiles in Figure 5 a.2. and a.3., have two peaks at values of Y approximately equal 0.2 and 0.8. These are attributed to the acceleration of the flow as it crosses the ribs at $Y = 0.1$ and 0.9 for the ribbed walls, respectively. In the region near the downstream wall, $X = 0.8$ (Figure 5 a.1.), the velocity profiles are close to a single shape. The velocity at the centreline is near 0.9. The two peaks in the rib region are between 1.3 and 1.6. The flow at the centreline of the passage, $X = 0.6$ and $Y = 0.5$, also has a streamwise velocity of approximately 0.9. The streamwise velocities in the peak regions vary from 1.25 to 1.6 or more. This large variation is attributed to measurement locations close to the ribs, e.g., $X = 2.63$. The streamwise velocities at $Z = 0.4$, have a common minimum of $U = 1.07$. The velocity profiles nearer the walls vary depending upon streamwise location as noted by Bonhoff, B. (1998).

The cross-stream velocity profiles (Figure 5 b.1., b.2., and b.3.) show a well-behaved increase in velocity as the fluid moves from the web or upstream wall to the outer or downstream wall. The peak velocities of 0.4 at $Z = 0.4$ increase to 0.65 at $Z = 0.8$.

The velocities normal to the ribbed walls (Figure 5 c.1., c.2., and c.3.) have a more complex shape, which reflects the secondary flow pattern caused by the ribs. The velocity directions near the walls, e.g., $Y = 0.1$ and 0.9 are compatible with the single large secondary flow cell.

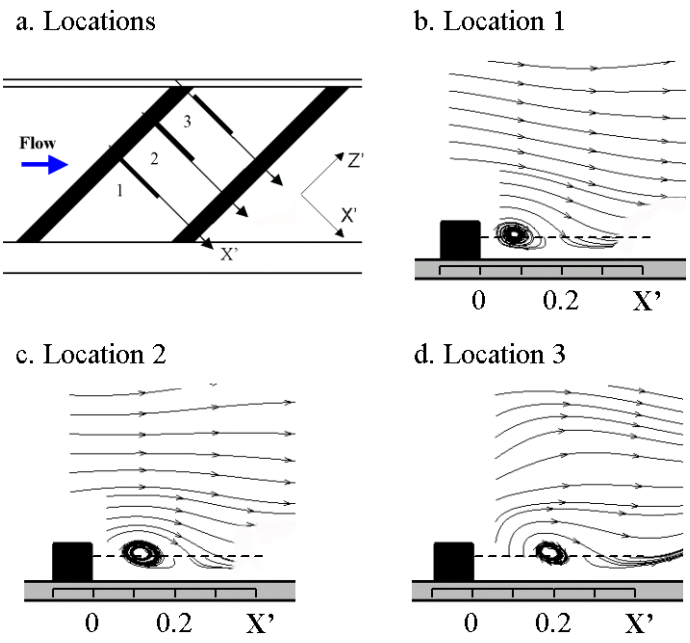

Figure 6: Streamline details in the vicinity of a rib.

Figure 6 shows streamline patterns over and downstream a rib in the 16th rib module. Data are extracted from measurement planes normal to the ribs. The streamlines are plotted along the local X'-axis. Due to reflection, no measurements are available in the vicinity of the walls and ribs.

As Z' increases from location 1 towards location 3, the recirculation cell evolves including the main stream flow above it, and the stagnation point on the bottom wall. The vortex centre moves from both the downstream edge of the rib and the ribbed wall. The recirculation cell size increases.

The vertical velocities at $Y = 0.06$ are shown in Figure 7 for the same planes as in Figure 6. The profiles are extracted from the plane $Y = 0.06$, represented by dashed lines in Figure 6. Note that negative and positive velocities indicate impinging flow and motion away from the wall, respectively.

As the flow moves along the rib from the web towards the outer wall, the recirculation cell increases in size as it moves from the downstream wall of the rib. The centre location of the vortex, characterised by V zero-values, are located at $X' = 0.11$ in plane-1 and at $X' = 0.19$ in plane-3. The angle of the vortex centreline to the ribs increases from 4deg between plane-1 and plane-2, to 11deg between plane-2 and plane-3. V minima, indicating impinging velocity maxima, are shifted away from the rib. The V minima shift angle increases from 7deg between plane-1 and plane-2, to 12deg between plane-2 and plane-3. The length of the negative velocity region, indicating the impinging area of the flow, also increases as the flow moves towards the outer wall. The absolute values of the impinging velocity decrease as the impinging area increases.

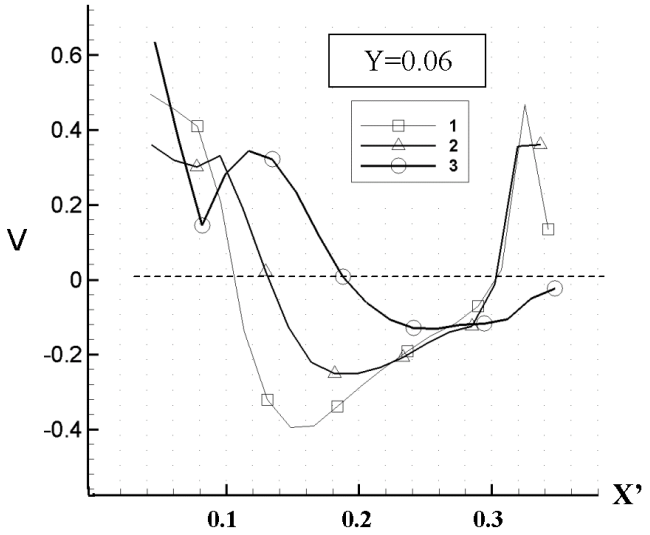

Figure 7: Velocity profiles downstream of a rib normal to the bottom wall (see Figure 6 for exact location).

The results presented in the previous section provide a set of measurements that can be used to evaluate codes and turbulent transport models in the developed flow region of a ribbed channel. This flow in this region is as "periodic" as will probably be obtained in most coolant channels. The data provide a good test for codes to predict flow and heat transfer with various turbulence models and wall approximations.

The upstream fully developed region extents from $X = 3.5$ to $X = 0.5$. The ribbed wall ($Y = 0$) and the outer wall ($Z = 1.1$) are shown. Note that the view direction goes through

the web, which is not plotted here to clarify the figure. Streamlines extracted from the full set of PIV measurements are plotted in Figure 8; they were chosen to start at several locations in order to identify characteristics of the flow field in the fully developed region. The streamline colour helps to distinguish the start location.

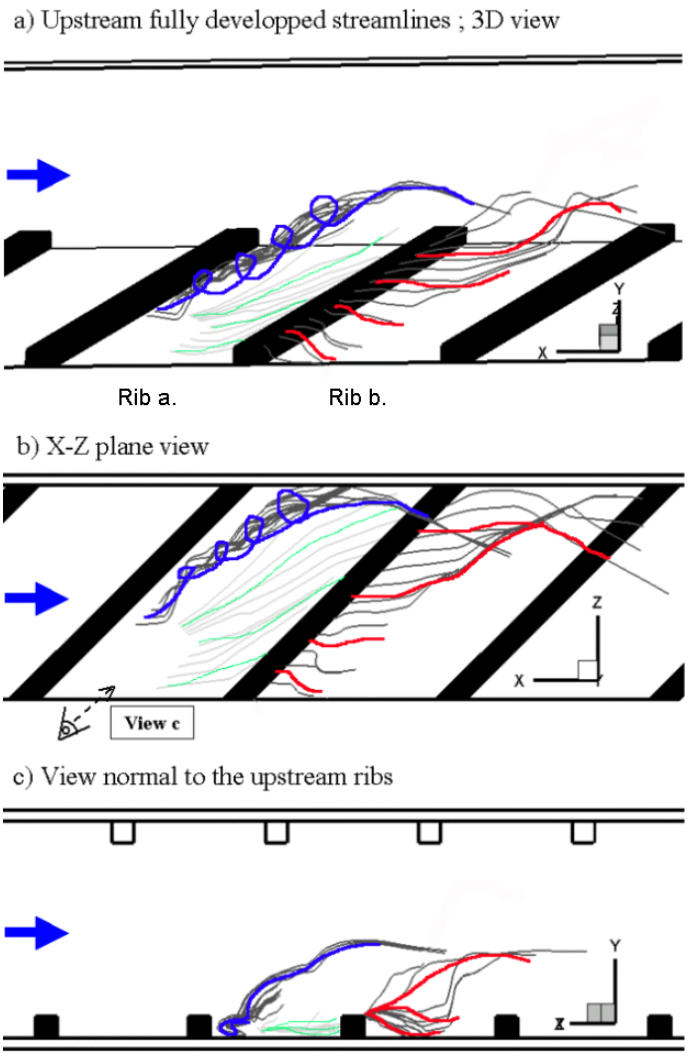

Figure 8: 3D-streamlines in the near bottom wall region.

Streamlines plotted downstream of the ribs show the location and size of the recirculation cell. In the rib-module-a, streamlines (blue) start in the core of the recirculating cell, pointing at the recirculating cell itself. In the rib-module-b, the streamlines (red) start just above the upper rib surface; they go over the recirculating cell and underline the flow reattachment downstream of the recirculating cell.

In the rib-module-a upstream corner between the rib and the web, a recirculating cell starts. As Z increases, the flow inside the recirculating cell is directed along the rib with a convective velocity of $1.2U_b$. The flow develops into a vortex shape along the rib; this is the rib-induced vortex typically mentioned in literature on heat transfer with 45deg rib arrangements. As also shown in Schabacker, J. (1998) and in Figure 6, the vortex size is increasing as the distance to the divider increases. The vortex centre is directed in the streamwise direction as Z increases, yielding in greater reattachment distances from the rib downstream wall. Figure 8 b. in rib a. shows the location of the vortex relative to the rib.

As the vortex is approaching the outer wall, the vortex strength decreases and the streamlines impinge on the outer wall. The streamlines from the bottom rib region are guided along the outer wall up to $Y = 0.5$, and meet the flow coming from the top wall. This produces two counter-rotating cells already described in Chanteloup, D. (2001) and shown on Figure 4. The streamlines go as a sheet in the centre of the channel, towards the web. They reach the web $2D_H$ downstream of the impact area on the outer wall.

The part of the flow located above the ribbed wall (green streamlines), between the reattachment line and the next rib, is divided in two regions, separated by a line linking the web-upstream rib corner and the outer wall-downstream rib corner. The part of the flow located upstream of this line undergoes the vortex influence and is directed towards the outer wall. This portion of the flow impinges on the outer wall in the region $1.9 > X > 2.4$, $Y < 0.3$. The part of the flow located downstream of the separation line, undergoes the effect of the mainstream flow. This region is characterised by low impingement. The flow is directed towards the downstream rib, with velocities parallel to the ribbed wall.

The conclusion from these data is that the complex flow induced by the 45deg rib arrangement causes the development of a secondary vortex behind each rib. The main source of the flow characteristics in the straight legs is the vortex induced by the ribs. This vortex structure must be accurately predicted to obtain accurate local heat transfer simulations from the CFD predictions. The previous sections give details that can be used to evaluate CFD calculations.

Heat transfer measurements

Heat transfer measurements were conducted in the same model to accompany the flow results. Following are data and discussion on the heat transfer results in the fully developed region (16^{th} and 17^{th} rib module).

Figure 9 shows the heat transfer distribution in the 16^{th} and 17^{th} rib modules, located at $3.5 > X > 1$ in the upstream leg. Two walls are shown, the bottom and the outer walls. Nu/Nu_0 contours are plotted, where Nu_0 is the Dittus-Boelter correlation value for a smooth channel: $Nu_0 = 0.023 \cdot \mathrm{Re}^{0.8} \cdot \mathrm{Pr}^{0.4}$; in the present study, $Nu_0 = 114.5$. The periodic heat transfer distribution from rib to rib shows the region's near fully developed. Small differences may also be attributed to the presence of the turn ($1D_H$ downstream).

On the ribbed wall, four regions can be identified in the rib-module heat transfer distribution. Along the upstream rib, an area of high heat transfer occurs. The Nu/Nu_0 ratio decreases from the web towards the outer wall. The maxima

values (up to six times Nu_0), are located between 0.1 to $0.2D_H$ from the rib downstream wall. The angle of the maxima line to the rib is approximately 14deg. Next to the outer wall, another region of relatively high heat transfer occurs; Nu/Nu_0 values reach 2.5. A similar region is located next to the downstream rib. Between these three regions, in the rib-module centre, low heat transfer occurs: The Nu/Nu_0 values are between 1 and 1.5, which are almost the same as in a smooth channel.

On the first side wall where the vortex impacts, two regions are clearly detectable. A region of high Nu/Nu_0 values is located at mid distance between the ribs. It is $0.5D_H$ long and occupies the space $0.3 > Y > 0$ on the outer wall. Nu/Nu_0 values are over 3 in this region. Small differences occur near the top wall due to the channel geometry. Around the channel centre plane ($Y = 0.5$), heat transfer is lower with Nu/Nu_0 values between 1 and 2.

Results on the same walls were presented in Rau, G. (1998) with a directly opposing 45deg rib arrangement. The distribution was similar to the present study on the bottom wall with the same order of magnitude of Nu/Nu_0. On the outer wall, some differences between the present results and Rau, G. (1998) occurred due to the symmetric, instead of the staggered rib arrangement in the present experiments.

Due to optical access restrictions, measurements on the web or second side wall weren't obtained in the first leg of the model. However, measurements were taken $10D_H$ downstream of the bend in the second leg of the model. The rib arrangement in the configuration is such that the web of the upstream leg and the downstream outer wall of the second leg, have a similar position, compared to the channel flow field. The ribbed wall heat transfer distributions in Figure 9 and Figure 10 are very similar and Chanteloup, D. (2001) showed that at $X = 4$, the flow has almost reached fully developed conditions. Thus measurements on the outer wall in the second leg (Figure 10) are representative of the upstream web heat transfer.

The differences between the side walls in Figure 9 and Figure 10 outer walls are noticeable. The heat transfer levels are much higher on the wall where the vortex, behind the ribs, impinges. Two regions are present: A low heat transfer region is located near the ribbed walls, with values $1 < Nu/Nu_0 < 1.5$. Around the centre line, a region of higher heat transfer values occurs ($1.5 < Nu/Nu_0 < 2$). Note that in Table 3, the downstream outer value is identified as *Sts web*.

Rau, G. (1998) also noted big differences between both smooth walls in its configuration. The 45deg rib arrangement leads to high inhomogeneous heat transfer between all channel walls; ribbed walls area-averaged values are 25% and 40% higher than the outer and web walls respectively. The conclusion is that the rib-induced flow has a great impact on the heat transfer distribution, between the ribs on the ribbed walls, and on the sidewalls.

Re= 50 000	**Results**	**Han**
Str	0.0091	0.0085
Sts outer	0.0073	0.0067
Sts web	0.0054	0.0067

Table 3: Fully developed area average Stanton numbers compared to Han, J. C. (1988) correlation.

Table 3 gives values of area-average Stanton number. Measurements were normalised by the projected area to compare with the correlations. *Str, Sts outer* and *Sts web* represent the ribbed wall, outer and web walls area average Stanton numbers respectively. Note that Han, J. C. (1988) smooth wall values were obtained as the mean value of both smooth walls. Present heat transfer results and correlations are in good agreement, taking into account the measurement and correlation uncertainties (±8% and ±10% respectively), and the blockage ratio differences between Han, J. C. (1988) and the present geometries.

Combination of flow and heat transfer measurements

3D-views of the flow streamlines superimposed on the heat transfer distribution are shown in Figure 11 and Figure 12. Note that for readability reasons, only seven Nu/Nu_0 contour values are plotted. This combination shows the strong influence of the rib-induced secondary flow on the heat transfer. Regions of high Nu/Nu_0 values can be explained by the shape and location of the rib-induced vortex. In Figure 11, the streamlines of Figure 8 b. are superimposed on the heat transfer distribution of Figure 9. Note that the symmetrical channel geometry, which yields to two separate flow regions placed around the $Y = 0.5$ plane, yields a symmetrical heat transfer distribution in the two channel regions: $Y < 0.5$ and $Y > 0.5$.

Near the web behind the rib, the vortex begins in the region of highest heat transfer, up to 6 times the smooth channel Dittus-Boelter correlation value. The vortex develops along the rib, it coincides on the bottom wall with the U-shape high heat transfer area behind the rib. The reattachment zone corresponds to the high heat transfer region on the bottom wall. The varying reattachment length leads to a high Nusselt number region at 30deg angle to the streamwise direction. This corresponds to the angle of the maximum impinging velocity shown in Figure 7. The decrease of the impinging velocity leads to a negative Nusselt number gradient in the Z direction. As the vortex impinges on the outer wall, another region of high heat transfer occur, yielding a high heat transfer area on the sidewall ($Nu/Nu_0 > 3$ for $Y < 0.3$). Around the $Y = 0.5$ plane on the outer wall, velocity vectors are away from the outer wall (Figure 4), which leads to a low heat transfer region.

Part of the flow, which is not directed in the rib-induced vortex, remains parallel to the walls. It induces lower heat transfer regions on the walls. The flow passes over the recirculating cell in the upstream rib vicinity, and goes towards the bottom wall in the middle of the rib-module. It induces a

region of low Nusselt number. Nu/Nu_0 values reach 1, which indicates that the heat transfer coefficient is approximately the same as in a smooth channel.

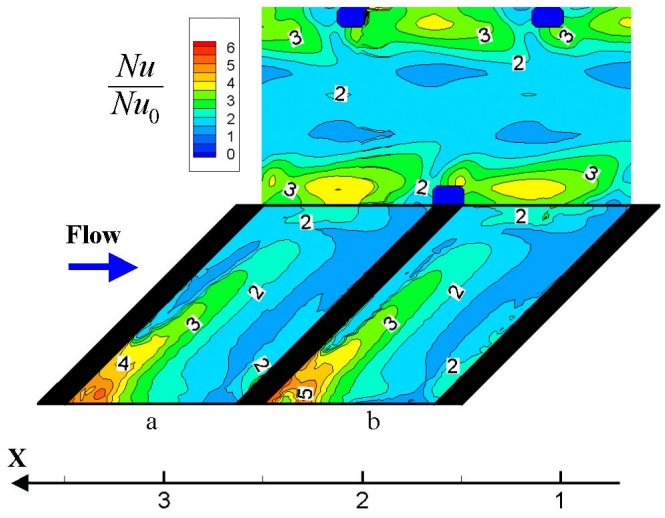

Figure 9: 2D-view heat transfer distribution on the bottom and outer walls in the fully developed region.

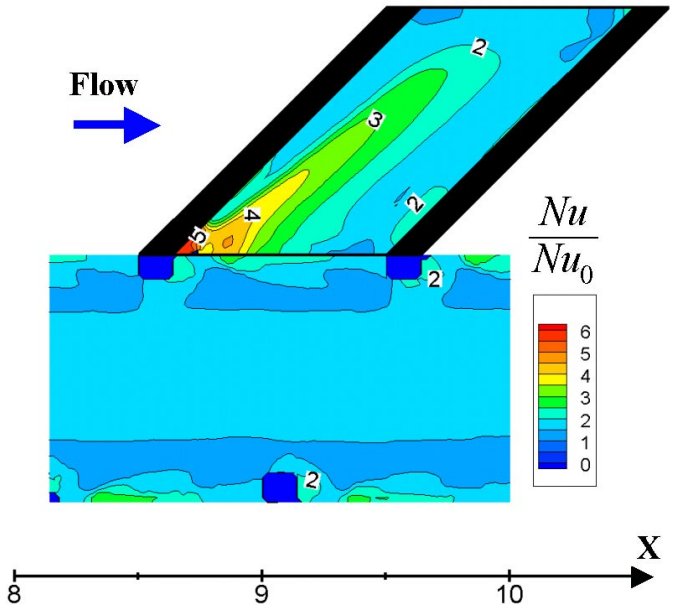

Figure 10: 2D-view heat transfer distribution on the bottom and outer walls, 10D_H downstream of the bend.

Figure 12 shows the same region with the heat transfer results of Figure 10 and with streamlines plotted from the centre of the channel. These streamlines are not previously shown. They are representative of the part of the flow that goes towards the web in the middle of the channel around the $Y = 0.5$ plane (see Figure 4). Two 2D views are added to Figure 12 to identify the streamline 3D locations (along *X-Y* and *X-Z* planes). The streamlines do not show any vortex in the middle of the channel. The flow crosses the channel as sheets parallel to the ribbed walls. The flow is smoothly directed towards the downstream direction by the mainstream motion. The impact on the web is weaker than on the outer wall. This explains the relatively low heat transfer coefficient on the web shown in Figure 10; Nu/Nu_0 values between 1 and 2 in the web centre part.

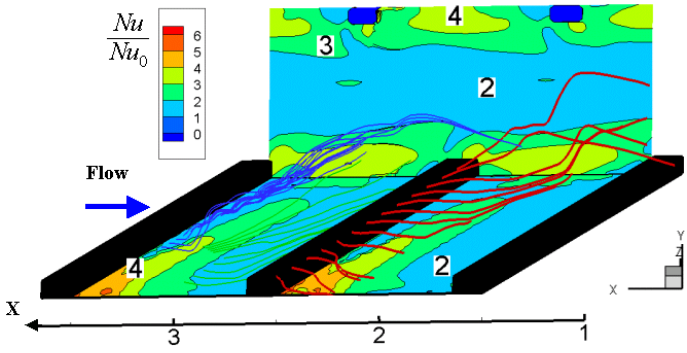

Figure 11: Combined heat transfer distribution and streamlines in the vicinity of the bottom and outer walls: 3D view.

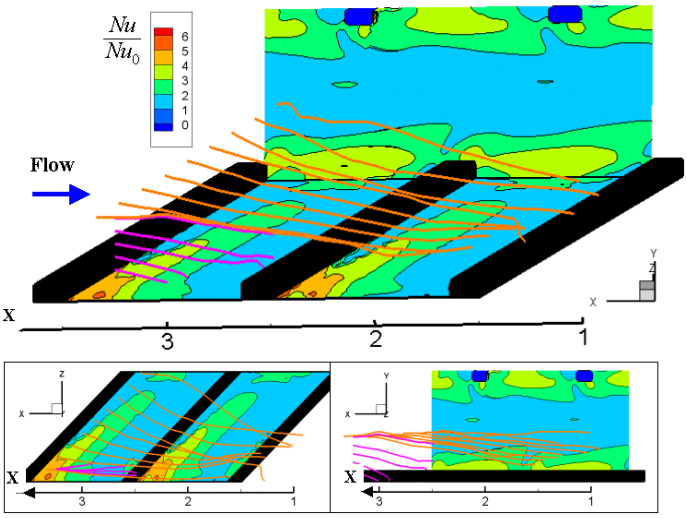

Figure 12: Combined heat transfer distribution and streamlines in the vicinity of the $Y = 0.5$ plane and web: 3D- and 2D-views.

CONCLUSIONS

Three-dimensional velocity measurements and heat transfer measurements were obtained in a two-legged blade coolant passage model with ribs orientated 45deg to the passage. The model length, the rib locations and the geometry of the web between the coolant passage legs was more representative of aero or land-based gas turbine cooling designs than previously available geometries. The results from these flow and heat transfer measurements were combined, to show the impact of the flow field on the heat transfer distribution in the fully developed region of a 2-pass internal coolant passage.

The measurements provide data to compare with CFD predictions, to evaluate mesh strategies, turbulence or wall treatment models.

Measurements in the developed flow region show details in the three velocity profiles. The measurements showed the tendency of the streamwise and cross-stream velocities to be similar for various streamwise locations at the same cross-stream location. The two secondary vortices in channel cross sections are due to the interaction of the rib induced and the mainstream flows. A secondary motion divides the flow along the channel into two separate regions. The flow in the two halves ($Y < 0.5$ and $Y > 0.5$) is constrained to remain in the same region along both straight legs.

A rib-induced vortex develops downstream of the ribs, impinges on the outer wall along the bottom wall, flows towards the top wall along the outer wall for $Y < 0.5$, and goes back towards the web along the $Y = 0.5$ plane. As the vortex develops along the rib, the vortex size increases, and the centre moves from the rib and from the ribbed wall.

Ribs at 45deg increase the average heat transfer gradients. Several regions of different heat transfer levels are identified on the ribbed and sidewalls. The ratio of high to low *Nu* numbers goes up to 6 in the U-shaped heat transfer distribution downstream of the ribs. High heat transfer gradients occur between the four channel walls in the area-averaged values between the walls (Table 3), which are required to cool the expected walls. Gradients also occur in the heat transfer distributions on each wall surface, which causes high temperature gradients and thermal stresses in the blade.

The complex phenomenon of the vortex and mainstream flow combination, which governs the heat transfer distribution in the straight legs of the coolant passage with inclined ribs have been connected from the combined flow and heat transfer measurements. The impinging velocity induced by the vortex, and more generally by the secondary flow, are strongly linked with the regions of high heat transfer. The present work provides results to understand how to use the secondary flow and especially the inclined rib-induced vortex, in order to reduce the high heat transfer gradients on the channel walls.

ACKNOWLEDGMENTS

This study was funded by the Swiss Office of Science in cooperation with the BriteEuram Internal Cooling of Turbine Blades project (contract number: BRPR-CT97-0600, project number: BE97-4022).

REFERENCES

1. Schabacker, J. (1998). *PIV investigation of the flow characteristics in an internal coolant passages of gas turbine airfoils with two ducts connected by a sharp 180° bend*. In: *PHD Thesis* (Ecole Polytechnique fédérale de Lausanne), Vol. n°1816.
2. Mochizuki, S., Murata, A. and Fukunaga, M. (1997). *Effects of rib arrangements on pressure drop and heat transfer in a rib-roughened channel with a sharp 180 deg turn.* Journal of Turbomachinery, 119 3, 610-616.
3. Han, J.C., Zhang, P. and Lee. (1991). *Augmented heat transfer in square channels with parallel, crossed, and V-shaped angled ribs.* Journal of Heat, 113 January 1991, 590-596.
4. Han, J.C. and Park, J.S. (1988). *Developing heat transfer in rectangular channels with rib turbulators.* Journal of Heat and Mass Transfer, 31 1988, 183-195.
5. Han, J.C. and Chandra, P.R., *Local Heat/Mass Transfer and Pressure Drop in a Two-Pass Rib-Roughened Channel for Turbine Airfoil Cooling*. 1987, Lewis Research Center NASA.
6. Wang, Z., Ireland, P.T., Kohler, S.T. and Chew, J.W. (1996). *Heat transfer measurements to a gas turbine cooling passage with inclined ribs*. Proceedings of the International Gas Turbine & Aeroengine Congress & Exhibition. Birmingham, UK. 1996. 96-GT-542.
7. Rau, G. (1998). *Einfluss der Rippenanordnung auf das Strömungsfeld und den Wärmeübergang in einem Kühlkanal mit quadratischem Querschnitt*. In: *PHD Thesis* (Technischen Universität Darmstadt), Vol. D17.
8. Schabacker, J., Bölcs, A. and Johnson, B.V. (1999). *PIV investigation of the flow characteristics in an internal coolant passage with 45° rib arrangement*. Proceedings of the International Gas Turbine & Aeroengine Congress & Exhibition. Indianapolis, Indiana, USA. 1999. 99-GT-120.
9. Schabacker, J., Bölcs, A. and Johnson, B.V. (1998). *PIV investigation of the flow characteristics in an internal coolant passage with two ducts connected by a sharp 180° bend*. Proceedings of the International Gas Turbine & Aeroengine Congress & Exhibition. Stockholm, Sweden. 1998. 98-GT-544.
10. Bonhoff, B., Schabacker, J., Parneix, S., Leusch, J., Johnson, B.V. and Bölcs, A. (1998). *Experimental and numerical study of developed flow and heat transfer in coolant channels with 45 and 90 degree ribs*. Proceedings of the Turbulent heat transfer II. Manchester, UK. 1998. 99-GT-123.
11. Hermanson, K., Parneix, S., Von Wolfersdorf, J. and Semmler, K. (2000). *Prediction of Pressure Loss and Heat Transfer in Internal Cooling Passages*. Proceedings of the Turbine-2000: International Symposium on Heat Transfer in Gas Turbine Systems. Cesme, Izmir, Turkey. 2000. 934, 448-455.
12. Schabacker, J. and Bölcs, A. (1996). *Investigation of Turbulent Flow by means of the PIV Method*. Proceedings of the 13th Symposium on Measuring Techniques for Transonic and Supersonic Flows in Cascades and Turbomachines. Zurich, Switzerland. 1996.
13. Wang, Z., Gillepsie, D.R.H. and Ireland, P.T. (1996). *Advances in heat transfer measurements using liquid crystals*. In: *Turbulent Heat Transfer* (Engineering Foundation), 1-25. San Diego.
14. Ekkad, S.V. and Han, J.C. (1995). *Local heat transfer distributions near a sharp 180° turn of a two-pass smooth*

square channel using a transient liquid crystal image technique. Journal of Flow Visualisation and Image Processing, 2, 285-297.
15. Vogel, G. and Bölcs, A. (2000). *A novel digital image processing system for the transient liquid crystal technique applied for heat transfer and film cooling measurements*. Proceedings of the International Symposium on Heat Transfer in Gas Turbine Systems. Izmir, Turkey. 2000.
16. Chanteloup, D. and Bölcs, A. (2001). *PIV investigation of the flow characteristics in 2-leg internal coolant passages of gas turbine airfoils*. Proceedings of the Euroturbo, 4th European conference on turbomachinery fluid dynamics and thermodynamics. Firenze, Italy. 2001.
17. Wang, Z. (1991). *The application of thermochromic liquid crystals to detailed turbine blade cooling measurements*. In: *Thesis* (Department of Engineering Science, Oxford).
18. Vogel, G. and Weigand, B. (2001). *A new evaluation method for transient liquid crystal experiments*. Proceedings of the National Heat Transfer Conference. Anaheim, California, USA. 2001. NHTC01-1511.
19. Bendat, J.S. and Piersol, A.G. (1986). *Random data*. In: *Random data* (John Wiley & Sons, Inc.).
20. Höcker, R. (1996). *Optimization of transient heat transfer measurements using thermochromic liquid crystals based on an error estimation*. Proceedings of the International Gas Turbine & Aeroengine Congress & Exhibition. Birmingham, UK. 1996. 96-GT-235.
21. Haasenritter, A., Amro, M. and Weigand, B. (2001). *An experimental and numerical study of the heat transfer performance of sharp-edged and rounded ribs in square ducts*. Proceedings of the The 9th International Symposium on Transport Phenomena and Dynamics of Rotating Machinery. Honolulu, Hawaii, USA. 2001.